
REArtGS: Reconstructing and Generating Articulated Objects via 3D Gaussian Splatting with Geometric and Motion Constraints

**Di Wu^{1,2}, Liu Liu^{3*}, Zhou Linli¹, Anran Huang³, Liangtu Song¹, Qiaojun Yu⁴,
Qi Wu^{4,5†}, Cewu Lu⁴**

1 Hefei Institutes of Physical Science Chinese Academy of Sciences

2 University of Science and Technology of China

3 Hefei University of Technology

4 Shanghai Jiao Tong University

5 ByteDance

Email: wdcs@mail.ustc.edu.cn, liuliu@hfut.edu.cn

Abstract

Articulated objects, as prevalent entities in human life, their 3D representations play crucial roles across various applications. However, achieving both high-fidelity textured surface reconstruction and dynamic generation for articulated objects remains challenging for existing methods. In this paper, we present REArtGS, a novel framework that introduces additional geometric and motion constraints to 3D Gaussian primitives, enabling realistic surface reconstruction and generation for articulated objects. Specifically, given multi-view RGB images of arbitrary two states of articulated objects, we first introduce an unbiased Signed Distance Field (SDF) guidance to regularize Gaussian opacity fields, enhancing geometry constraints and improving surface reconstruction quality. Then we establish deformable fields for 3D Gaussians constrained by the kinematic structures of articulated objects, achieving unsupervised generation of surface meshes in unseen states. Extensive experiments on both synthetic and real datasets demonstrate our approach achieves high-quality textured surface reconstruction for given states, and enables high-fidelity surface generation for unseen states. Project site: <https://sites.google.com/view/reartgs/home>.

1 Introduction

Articulated objects are ubiquitous in our daily lives. Modeling articulated objects, i.e. mesh reconstruction and generation, holds significant importance in many fields of computer vision and robotics fields including virtual and augmented reality [16, 34], object manipulation [38, 30] and human-object interaction [35, 12]. Currently, the surface and shape reconstruction for articulated objects is a non-trivial task due to the challenges: firstly, articulated objects exhibit complicated and diverse geometric structures with a wide range of scales. Secondly, articulated objects possess varied kinematic structures, and the static surface meshes generated from vanilla 3D reconstruction methods fail to meet practical interaction requirements. Under this circumstance, PARIS [14] attempts to use multi-view images from two states for articulated object dynamically reconstruction with neural implicit radiance fields. Nevertheless, PARIS lacks geometric constraints, leading to shape-radiance ambiguity and additional errors for motion analysis.

*Corresponding author

†Project leader

In recent years, 3D Gaussian Splatting (3DGS) [10] achieves realistic and real-time novel view synthesis through explicit representation with 3D Gaussian primitives. Some subsequent works have expanded 3DGS to surface reconstruction [40, 8, 1] and dynamic reconstruction [36, 13, 4]. However, existing 3DGS-based surface reconstruction methods typically suffer from insufficient geometric constraints [40] or impose constraints by restricting the shapes of Gaussian primitives [8, 6], leading to noisy surface reconstruction results. On the other hand, current dynamic reconstruction methods via 3DGS tend to input motion time and spatial positions into neural networks to obtain the deformed positions of Gaussian primitives [36, 4]. Consequently, these methods require continuous supervision throughout the entire motion, which limits their ability to generate surface meshes in unseen states. In general, introducing 3DGS as a ready-to-use technique into articulated object surface reconstruction and generation is still not feasible and remains a challenging task.

In this paper, to address the aforementioned issues and make full advantage of 3DGS, we propose **REArtGS**, a novel approach that **R**econstructs and **E**Generates high-quality texture-rich mesh surfaces for **A**rticulated objects via **3D G**aussian **S**

Subsequently, we employ the optimized Gaussian primitives as an accurate geometry initialization for dynamic surface generation. Due to the absence of intermediate states, we leverage the kinematic structures of articulated objects to model time-continuous Gaussian deformable fields in an unsupervised fashion, and constrain the deformable fields using learnable motion parameters. Concretely, we propose a heuristic method for unsupervised part segmentation and formulate the deformable fields of dynamic parts via the motion parameters. Our REArtGS is evaluated on PartNet-Mobility [32] and AKB-48 [15] object repositories, ranging from synthetic to real-world data. Extensive experiments demonstrate that our REArtGS outperforms existing state-of-the-art methods in articulated object surface reconstruction and generation tasks, as shown in Fig. 1.

In summary, our main contributions can be summarized as follows: (1) We propose REArtGS, a novel framework introducing 3DGS to conduct high-quality textured surface reconstruction and time-continuous generation for articulated objects, only using multi-view images from two arbitrary states. (2) Our REArtGS exploits an unbiased SDF guidance for 3D Gaussian primitives to enhance geometric constraints for improving reconstruction quality, and also establishes the deformable fields constrained by kinematic structures of articulated objects to generate unseen states in an unsupervised manner. (3) We incorporate REArtGS into various scenes ranging from synthetic to the real-world data across many different articulation categories. The extensive experimental results demonstrate that our approach significantly outperforms SOTAs in both mesh reconstruction and generation tasks.

2 Related Work

2.1 Articulated Object Shape Reconstruction

Object surface reconstruction is a well-established problem for understanding the full geometric shape of objects. Some works introduce to encode continuous functions that model the objects using Signed Distance [23, 21], radiance [20, 26, 29] and occupancy [19]. To achieve both geometry and motion analysis in a single forward, Ditto [9] and REACTO [28] propose to generate shapes at unseen states from pair observations. Specifically, PARIS [14] alleviates the 3D data requirement

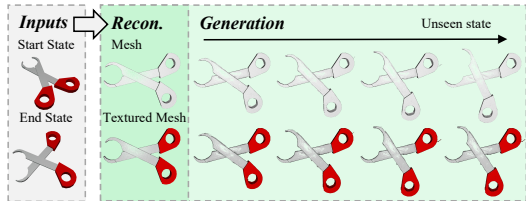


Figure 1: Given multi-view RGB images of articulated objects from two arbitrary states, our REArtGS enables high-quality textured surface mesh reconstruction and generation for unseen states.

limitation and succeeds in reconstructing shape surface with only RGB images. Most recently, ArticulatedGS [7] and ArtGS [17] introduce 3DGS to achieve both the reconstruction and motion estimation of articulated objects. However, these methods still suffer from insufficient geometry constraints, which may lead to noisy surface mesh outputs. Therefore, our REArtGS aims to address these issues, and proposes geometric and motion constrained 3DGS for this task.

2.2 Surface Reconstruction with 3DGS

3D Gaussian Splatting has become increasingly popular technique for surface reconstruction in recent years [10, 11, 39, 25]. GOF [40] establishes opacity fields of 3D Gaussians using ray-tracing-based rendering, and extracts the surface meshes by the opacity level set. 2DGS [8] and PGSR [1] seek to transform 3D Gaussians into 2D flat representation, obtaining accurate normal distribution. Although improving the surface reconstruction quality, these methods still lack more reasonable geometry constraints. Several researchers attempt to integrate SDF representation with 3D Gaussians [37, 2, 33, 3], but these approaches commonly use SDF to regularize normals and guide the pruning of 3D Gaussians, without substantial optimization of Gaussian opacity fields. Meanwhile, some works conduct dynamic reconstruction using 3DGS. Deformable 3DGS proposes a deformation field to reconstruct dynamic scenes with 3D Gaussian primitives. 4DGS [4] leverages a spatial-temporal structure encoder and a multi-head Gaussian deformation decoder to derive the deformed 3D Gaussians at a given time. However, these methods rely on complete supervision of the motion process, limiting their capacity for generating unseen states. The similar issues also occur in DGMesh [13] and REACTO [28]. We provide more analysis and comparison of the related works in Appendix B.

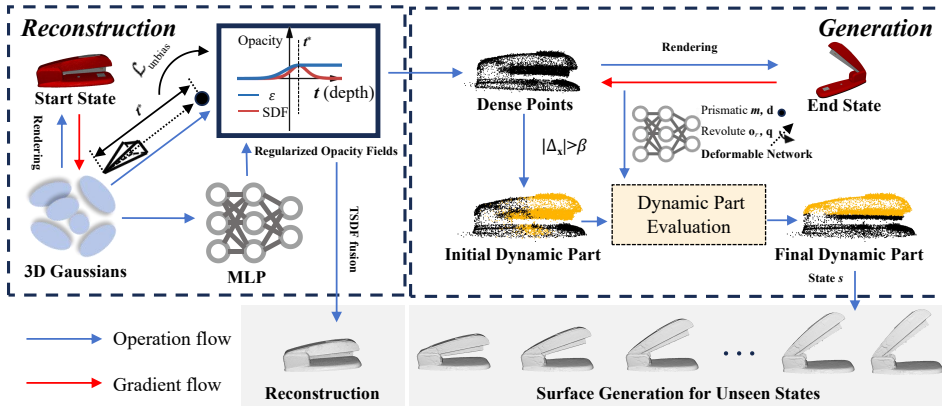


Figure 2: The overall pipeline of REArtGS. We introduce additional geometric and motion constraints for 3D Gaussian primitives, achieving high-quality surface mesh reconstruction and time-continuous generation, with only multi-view images from arbitrary two states.

3 Method

The overall framework of our REArtGS is illustrated in Fig. 2. Taking multi-view RGB images from two arbitrary states $s = 0, s = 1$ of articulated objects, we aim to achieve high-quality textured mesh reconstruction and generation at any unseen states between $s \in [0, 1]$.

We first introduce SDF representation and propose an unbiased SDF regularization to enhance the geometry constraints of 3D Gaussian primitives. In this manner, we improve the reconstruction quality and yield dense point clouds at state $s = 0$, providing an accurate geometric prior for subsequent dynamic reconstruction. Then we establish time-continuous deformable fields for 3D Gaussian primitives constrained by the kinematic structures of articulated objects. Given any state s , we can derive the deformed position x_s of Gaussian primitives through the deformation fields in an unsupervised fashion. The details of our approach are elaborated below.

3.1 Reconstruction with Unbiased SDF Guidance

To better preserve the geometric features of Gaussian primitives, we use the ray-tracing-based 3DGS following GOF, which evaluates rendering contribution of Gaussian primitives directly without the 3D-to-2D projection step. However, the Gaussian primitives still suffer from insufficient geometric constraints. Concretely, the opacity fields lack an explicit link with scene surface, which may lead to noisy outputs in surface reconstruction of articulated objects.

To address the limitation, we first introduce SDF representation to guide the geometry learning of Gaussian primitives. We utilize a Multi-layer Perceptrons (MLP) with 8 hidden layers to learn the SDF values for spatial position inputs, and the scene surface can be represented by the zero-set:

$$\mathcal{S} = \{\mathbf{x} \in \mathbb{R}^3 \mid f(\mathbf{x}) = 0\} \quad (1)$$

Following Neus [31], we can derive the opacity $\hat{\sigma}$ for the center \mathbf{x}_i of Gaussian G_i from learned SDF values:

$$\hat{\sigma}_i = \max \left(\frac{\Phi(f(\mathbf{x}_i)) - \Phi(f(\mathbf{x}_{i+1}))}{\Phi(f(\mathbf{x}_i))}, 0 \right) \quad (2)$$

where Φ denotes a Sigmoid function. $f(\mathbf{x}_{i+1})$ is approximated as:

$$f(\mathbf{x}_{i+1}) = f(\mathbf{x}_i) + f'(\mathbf{x}_i) \Delta \mathbf{x} \quad (3)$$

where $\Delta \mathbf{x} = R S \mathbf{r}$. $R \in \mathbb{R}^{3 \times 3}$ is the rotation matrix derived from Gaussian's quaternion, and $S \in \mathbb{R}^{3 \times 3}$ is the diagonal matrix of Gaussian's scaling. \mathbf{r} is the normalized ray direction. Nevertheless, the SDF-opacity conversion is not directly applicable to the α blending rendering. This is because each 3D Gaussian primitive models a local density distribution, while Eq. 2 only maps the global positions to their opacity values and neglects the local properties of Gaussian primitives. Therefore, we define the opacity of Gaussian primitive combining the rendering contribution ε proposed in GOF as:

$$\begin{aligned} \sigma_i &= \hat{\sigma}_i \varepsilon(G_i) \\ &= \hat{\sigma}_i \cdot \max(e^{-\frac{1}{2} \mathbf{x}_L^T \mathbf{x}_L}) \\ &= \hat{\sigma}_i \cdot \max(e^{-\frac{1}{2} (\mathbf{r}_L^T \mathbf{r}_L t^2 + 2 \mathbf{o}_L^T \mathbf{r}_L t + \mathbf{o}_L^T \mathbf{o}_L)}) \end{aligned} \quad (4)$$

where $\mathbf{o}_L, \mathbf{r}_L$ are the camera center and incident ray direction represented in the local coordinate system of Gaussian G_i , which can be acquired by local scaling matrix and rotation matrix of G_i . The maximum value of $\varepsilon(G_i)$ occurs at ray depth t^* , expressed as follows:

$$t^* = \frac{\mathbf{o}_L^T \mathbf{r}_L}{\mathbf{r}_L^T \mathbf{r}_L} \quad (5)$$

The rendering equation based on σ is represented as:

$$\mathbf{C} = \sum_{i=1}^N \mathbf{c}_i \sigma_i \prod_{j=1}^{i-1} (1 - \sigma_j) \quad (6)$$

where N is the number of Gaussian primitives involved in α -blending and \mathbf{c}_i is the color modeled with spherical harmonics. To leverage SDF to constrain the geometric learning of Gaussian primitives, we first introduce a bell-shaped function Φ_k to modulate the transformation from SDF to opacity and replace the original Sigmoid activation function Φ in Eq. 2, formulated as:

$$\Phi_k(f(\mathbf{x})) = \frac{e^{k \cdot f(\mathbf{x})}}{(1 + e^{k \cdot f(\mathbf{x})})^2} \quad (7)$$

where k is a learnable parameter that adjusts the function shape and we initially set it to 0.1. Intuitively, the Gaussian primitive closer to the surface has a higher opacity value.

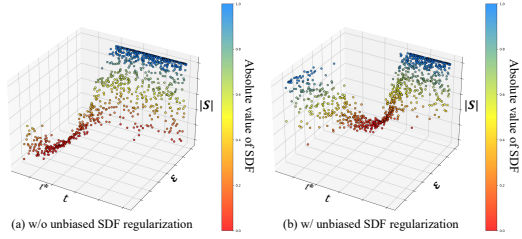


Figure 3: The illustration of unbiased SDF regularization. It can be observed that when t approaches t^* , the absolute value of SDF $|\mathcal{S}|$ converges to zero with the unbiased SDF regularization.

However, since $\hat{\sigma}$ is determined solely by the Gaussian's center, a non-alignment still exists between the maximum points of $\hat{\sigma}$ and ε , which can be formulated as:

$$t_{\text{bias}} = \left\| \underset{t}{\operatorname{argmax}}(\hat{\sigma}) - \underset{t}{\operatorname{argmax}}(\varepsilon) \right\| \quad (8)$$

To mitigate this bias, we propose an unbiased regularization for the SDF value at depth t^* as following:

$$\mathcal{L}_{\text{unbias}} = \|f(\mathbf{o} + t^*\mathbf{r})\|_2^2 \quad (9)$$

where \mathbf{o}, \mathbf{r} are the camera center and incident ray direction. Through the unbiased regularization, we encourage that when the rendering contribution of a Gaussian primitive reaches its maximum value, the corresponding spatial position is close to the scene surface, as shown in Fig. 3. In this manner, the SDF representation is able to regularize the opacity fields without bias and facilitate more reasonable distribution of Gaussian primitives over scene surface. We provide more detailed elaboration and proof in the Appendix C.1.

3.2 Mesh Generation with Motion Constraints

Due to the explicit representation of Gaussian primitives, we can acquire accurate dense point clouds from reconstruction, serving as initial geometry for mesh generation. Then we establish time-continuous deformable fields for 3D Gaussians to infer the deformed position \mathbf{x}_s at state s . However, it is challenging to optimize the deformable fields for Gaussian primitives only with the supervision of two states. Accordingly, we exploit the kinematic structures of articulated objects to constrain the Gaussian deformation field. We first assume that the articulated motion only includes rotation and translation following PARIS. Then we employ a heuristic method to efficiently predict the joint type through movement trend of points, which is elaborated in the Appendix C.3. For rotation joints, our learning objective is to determine their rotation axis and rotation angle. Specifically, we take the pivot point $\mathbf{o}_r \in \mathbb{R}^3$ of the rotation axis and a normalized quaternion $\mathbf{q} \in \mathbb{R}^4$ as learnable parameters, where the quaternion can be decoupled into the rotation axis $\mathbf{a} \in \mathbb{R}^3$ and rotation angle θ . For prismatic joints, our learning objective is to determine their translation directions \mathbf{d} and translation distances m . Similarly, we take the unit vector $\mathbf{d} \in \mathbb{R}^3$ representing the translation direction and the translation distance m as learnable parameters.

Subsequently, we formulate the deformable fields through a canonical state. Given the rotation motion $SO(3) \in \mathbb{R}^{3 \times 3}$, we define its canonical state as $s^* = 0.5$ and the rotation angle of state s can be expresses as:

$$\theta_s = \frac{(s^* - s)}{s^*} \theta \quad (10)$$

where $s \in [0, 1]$ and $\theta \in [-\pi/2, \pi/2]$. The angle-bounded parameterization is able to prevent the singularity in exponential coordinates when $\|\theta\| > \pi$. Using Rodrigues' rotation formula [24], the deformed position \mathbf{x}_s can be derived as following:

$$\mathbf{x}_s = (\mathbf{I} + \sin(\theta_s)\mathbf{K} + (1 - \cos(\theta_s))\mathbf{K}^2)(\mathbf{x} - \mathbf{o}_r) + \mathbf{o}_r \quad (11)$$

where \mathbf{K} is a skew-symmetric matrix formed by the rotation rotation axis \mathbf{a} and $\mathbf{I} \in \mathbb{R}^{3 \times 3}$ is a unit matrix. Meanwhile, we align the local quaternions of 3D Gaussian primitives after rotation through quaternion multiplication.

For the prismatic motion $m \cdot \mathbf{d} \in \mathbb{R}^3$, we take advantage of the vector space structure of Euclidean geometry by setting $s^* = 0$. The deformed position \mathbf{x}_s can be naturally acquired by linear interpolation, formulated as:

$$\mathbf{x}_s = \mathbf{x} + s \cdot m \cdot \mathbf{d} \quad (12)$$

unlike rotation motion, this parameterization avoids singularities due to the flat Riemannian structure of \mathbb{R}^3 .

However, the deformable fields should be applied exclusively to movable Gaussian primitives. Consequently, the Gaussian primitives need to be segmented into dynamic and static parts. To address this challenge, we propose an unsupervised method for dynamic part segmentation. We first only input the multi-view images at the end state during warm-up training iterations, and then perform an initialization segmentation of the dynamic part. The segmentation criterion for the initial dynamic

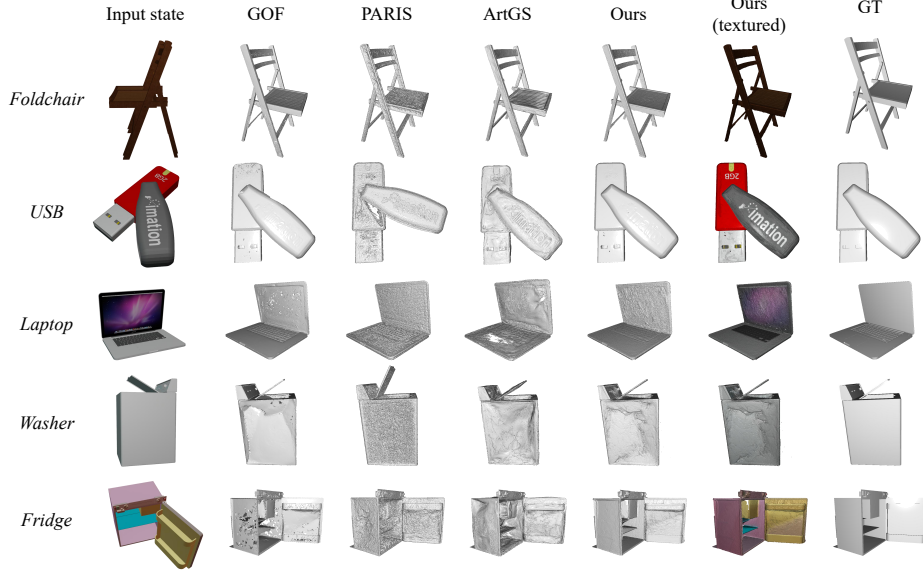


Figure 4: The qualitative result of surface reconstruction on PartNet-Mobility dataset. We show both textured and non-textured meshes for the best comparison.

components is represented as: $|\Delta_x| > \beta$, where $|\Delta_x|$ is the L1 distance of spatial position variation during the warm-up training, and β is its average value. Furthermore, the spatial transformation of the dynamic part should align with the learnable motion parameters. Hence the dynamic part among the Gaussian primitives is re-evaluated at certain intervals of iterations, where the criterion for revolute or prismatic joints is represented as:

$$\begin{aligned} |\hat{\theta} - \theta| &< \frac{\varphi_\theta}{K} \\ |\hat{m} - m| &< \frac{\varphi_m}{K} \end{aligned} \quad (13)$$

where $\hat{\theta}$, \hat{m} are the rotation angle around axis a and the translation distance respectively, φ is the tolerance threshold which decreases as the number of iterations K increases.

Moreover, our method can be conveniently transferred to multi-part articulated objects, through sequentially learning the segmentation masks and motions of each individual part. Please refer to our Appendix C.4 for more details.

3.3 Optimization and Textured Mesh Extraction

Since the shapes of Gaussian primitives are not limited, the normal distributions of Gaussian primitives are difficult to estimate accurately. However, Gaussian's normals should be parallel to the gradients of SDF in an ideal case. We consequently introduce additional regularization to regularize the normals of Gaussian primitives by SDF representation, expressed as follows:

$$\mathcal{L}_{\text{normal}} = \frac{1}{N} \sum_i^N \left(1 - \frac{|\mathbf{n}_i \cdot \nabla f(\mathbf{x}_i)|}{\|\mathbf{n}_i\| \cdot \|f(\mathbf{x}_i)\|} \right) \quad (14)$$

where \mathbf{n}_i represents the normal of Gaussian G_i , which is calculated following GOF:

$$\mathbf{n}_i = -R_i^T S_i^{-1} \mathbf{r}_L \quad (15)$$

where R is the rotation matrix encoded by Gaussian's quaternion and S is the scaling matrix. We also employ the Eikonal regularization term [5] to encourage SDF gradient direction perpendicular to the surface, represented as:

$$\mathcal{L}_{\text{eik}} = \frac{1}{N} \sum_{i=1}^N (\|\nabla f(\mathbf{x}_i)\|_2 - 1)^2 \quad (16)$$

The overall training objective \mathcal{L} is formulated as follows:

$$\mathcal{L} = \mathcal{L}_c + \lambda_1 \mathcal{L}_{\text{unbias}} + \lambda_2 \mathcal{L}_{\text{normal}} + \lambda_3 \mathcal{L}_{\text{eik}} + \lambda_3 \mathcal{L}_d \quad (17)$$

where λ is the weight of regularization and \mathcal{L}_d is the depth distortion loss following [8]. \mathcal{L}_c is defined as:

$$\mathcal{L}_c = \lambda \mathcal{L}_{\text{D-SSIM}} + (1 - \lambda) \mathcal{L}_1 \quad (18)$$

where $\mathcal{L}_{\text{D-SSIM}}$ is proposed in [10] and \mathcal{L}_1 is the L1 norm of the pixel loss.

Once the optimization converges, we adopt the TSDF fusion algorithm[22] to extract the textured mesh from Gaussian primitives. We utilize the α -blending rendering pipeline to obtain depth, opacity and RGB renderings for training views. Then we integrate these images into a voxel block grid (VBG) and extract a triangle mesh from the VBG. The textures of surface meshes can be efficiently obtained leveraging the spherical harmonics and opacity of Gaussian primitives. Please refer to our Appendix C.3 for a more detailed illustration.

Table 1: Quantitative results for the surface reconstruction quality on PartNet-Mobility dataset. We bold the best results and underline the second best results. * means we implement it without depth supervision for fair comparison.

Metrics	Method	Stapler	USB	Scissor	Fridge	Foldchair	Washer	Blade	Laptop	Oven	Storage	Mean
CD(ws) ↓	A-SDF [21]	14.19	7.14	10.61	13.71	40.85	12.50	3.31	2.11	21.37	22.57	14.84
	Ditto [9]	2.38	2.09	1.70	2.16	6.80	7.29	42.04	0.31	2.51	3.91	7.19
	PARIS [14]	0.96	<u>1.80</u>	<u>0.30</u>	2.68	0.42	18.31	0.46	0.25	6.07	8.12	<u>3.94</u>
	GOF [40]	<u>1.51</u>	8.09	0.36	<u>1.51</u>	0.53	17.35	0.89	0.84	19.81	10.04	6.09
	ArtGS* [17]	2.77	1.36	0.75	2.01	<u>0.41</u>	20.59	<u>0.63</u>	0.99	9.01	9.00	4.75
	REArtGS (Ours)	3.47	0.75	0.29	1.50	0.40	<u>12.20</u>	0.72	0.53	8.89	8.27	3.79
CD(rs) ↓	A-SDF [23]	<u>2.140</u>	2.478	1.805	1.801	2.080	1.590	5.630	2.418	2.751	4.077	2.677
	Ditto [9]	2.874	3.049	2.926	1.550	0.925	<u>1.428</u>	5.792	1.184	1.296	2.837	2.386
	PARIS [14]	2.077	3.812	2.807	0.370	1.209	3.869	2.855	1.025	2.873	2.903	2.380
	GOF [40]	2.510	1.736	2.304	2.230	2.787	5.725	<u>2.111</u>	<u>0.961</u>	3.080	2.812	2.626
	ArtGS* [17]	2.949	1.704	2.438	0.725	0.615	2.874	2.031	1.182	1.148	1.157	<u>1.682</u>
	REArtGS (Ours)	2.186	1.433	<u>2.291</u>	<u>0.475</u>	0.018	1.204	2.596	0.038	0.784	<u>1.330</u>	1.236
F1 ↑	A-SDF [23]	0.041	0.035	0.094	0.019	0.053	0.046	0.224	0.001	0.010	0.015	0.054
	Ditto [9]	0.197	0.181	0.275	0.114	0.352	0.059	0.107	0.366	0.052	0.030	0.173
	PARIS [14]	0.240	0.151	0.343	0.091	0.429	0.024	0.396	0.533	0.031	0.033	0.227
	GOF [40]	0.217	0.189	0.614	0.173	0.480	0.087	0.386	0.303	0.049	0.036	0.253
	ArtGS* [17]	<u>0.251</u>	<u>0.209</u>	0.438	0.118	0.447	0.053	<u>0.408</u>	0.294	<u>0.056</u>	0.042	0.232
	REArtGS (Ours)	0.256	0.307	0.598	0.165	0.502	0.069	0.488	0.419	0.065	0.066	0.294
EMD ↓	A-SDF [23]	0.755	1.113	0.952	0.945	1.020	0.982	1.763	1.039	1.174	1.258	1.100
	Ditto [9]	1.724	1.308	1.212	0.619	0.935	<u>0.841</u>	1.996	0.417	<u>0.852</u>	0.970	1.087
	PARIS [14]	1.197	1.381	0.637	0.426	0.778	1.660	1.823	0.706	1.200	1.046	1.085
	GOF [40]	1.643	1.815	1.075	1.055	1.181	1.692	1.237	<u>0.394</u>	1.241	0.959	1.229
	ArtGS* [17]	1.921	0.677	<u>0.934</u>	0.637	<u>0.506</u>	1.154	<u>1.131</u>	0.502	1.006	<u>0.787</u>	<u>0.926</u>
	REArtGS (Ours)	1.060	<u>0.847</u>	1.078	<u>0.485</u>	<u>0.097</u>	<u>0.777</u>	1.112	<u>0.111</u>	<u>0.627</u>	<u>0.755</u>	0.695

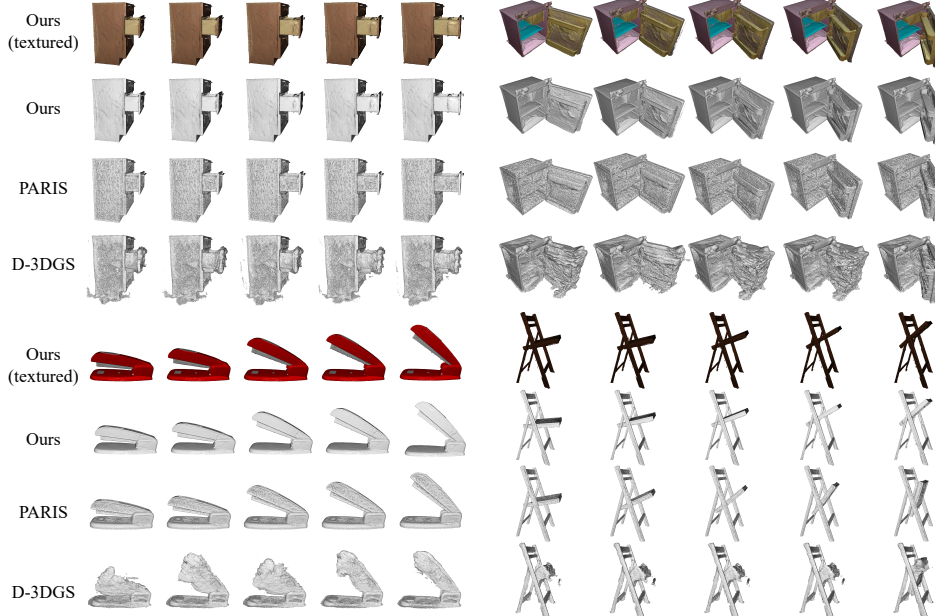


Figure 5: The qualitative results of surface generation at arbitrary unseen states on PartNet-Mobility dataset. We show both textured and non-textured meshes for best comparison. The states are sampled randomly.

Table 2: Quantitative results for the surface generation quality on PartNet-Mobility dataset. We bold the best results and underline the second best results. * means we implement it without depth supervision for fair comparison.

Metrics	Method	Stapler	USB	Scissor	Fridge	Foldchair	Washer	Blade	Laptop	Oven	Storage	Mean
CD(ws) ↓	A-SDF [21]	112.30	34.01	94.11	33.46	56.73	55.82	3.78	27.64	29.60	25.30	47.28
	PARIS [14]	2.09	14.51	12.81	2.64	10.42	<u>18.30</u>	0.80	<u>3.25</u>	10.89	5.89	8.16
	D-3DGS [36]	98.90	16.79	91.84	48.78	30.10	30.93	1.262	65.11	22.39	18.79	42.49
	ArtGS* [17]	<u>2.34</u>	<u>1.72</u>	0.68	2.05	<u>0.52</u>	20.59	0.63	1.00	8.78	10.97	<u>4.92</u>
	REArtGS (Ours)	2.60	1.68	0.44	2.21	<u>0.41</u>	14.80	<u>0.59</u>	3.65	8.11	6.48	4.10
CD(rs) ↓	A-SDF [21]	8.992	1.806	1.822	5.166	5.668	7.050	5.991	2.710	5.245	7.794	5.224
	PARIS [14]	2.113	0.417	4.704	4.08	1.216	0.857	4.442	1.354	<u>2.793</u>	4.332	2.264
	D-3DGS [36]	9.589	1.544	0.891	0.465	<u>1.147</u>	3.218	0.168	<u>0.449</u>	3.773	3.100	2.434
	ArtGS* [17]	4.924	0.670	0.381	0.471	1.622	2.670	1.455	1.269	3.912	0.562	1.794
	REArtGS (Ours)	3.651	0.487	0.127	0.464	0.420	1.617	0.414	0.298	2.129	1.020	1.063
F1 ↑	A-SDF [21]	0.007	0.034	0.056	0.012	0.021	0.023	0.168	0.001	0.010	0.004	0.034
	PARIS [14]	0.221	0.151	0.319	0.091	0.423	0.024	0.421	0.530	0.031	0.032	0.224
	D-3DGS [36]	0.064	0.180	0.125	0.073	0.168	0.195	0.233	0.131	0.022	0.023	0.121
	ArtGS* [17]	0.264	0.255	0.454	<u>0.125</u>	<u>0.460</u>	<u>0.055</u>	0.426	0.292	<u>0.062</u>	<u>0.045</u>	0.244
	REArtGS (Ours)	0.254	0.215	0.577	0.186	0.465	0.052	0.509	0.608	0.065	0.050	0.298
EMD ↓	A-SDF [21]	<u>2.123</u>	0.951	0.955	1.606	1.684	1.878	1.731	1.115	1.620	1.837	1.559
	PARIS [14]	2.454	0.457	1.533	0.451	0.780	0.655	1.491	0.770	1.183	1.354	1.113
	D-3DGS [36]	3.224	0.612	0.665	0.481	0.758	1.269	0.291	<u>0.436</u>	1.374	1.206	1.032
	ArtGS* [17]	2.207	0.562	<u>0.412</u>	0.563	<u>0.525</u>	1.171	0.631	0.724	1.297	<u>0.750</u>	0.884
	REArtGS (Ours)	1.594	0.494	0.251	<u>0.473</u>	0.459	0.900	<u>0.456</u>	<u>0.353</u>	<u>1.033</u>	<u>0.689</u>	0.670

4 Experiments

4.1 Experimental Setting

Datasets. To evaluate the reconstruction quality of our method, we conduct surface reconstruction experiments on synthetic dataset PartNet-Mobility [32] and real-world dataset AKB-48 [15], an extremely rich repository of real-world articulated objects which exhibit a wide variety of geometries and textures. Please see the Appendix D.1 for more details.

Metrics. Chamfer Distance (CD), F1-score and Earth Mover’s Distance (EMD) [41] are usually adopted as evaluation metrics for surface quality. However, these methods typically focus on the whole surface, endowing the unseen areas (such as the bottom of the object) with considerable weights during evaluation. This is unreasonable since we tend to be more concerned with the upper hemisphere regions of articulated objects. Therefore, we sample point clouds from the fragments between the rays cast by test cameras and the surface mesh to calculate EMD and CD, defined as CD (rs). We also evaluate the F1-score and CD for the whole surface, defined as CD (ws), to comprehensively evaluate the surface quality. Note that the CD values are multiplied by 1000 and the distance threshold of F1-score is set to 0.4. The calculation of these metrics can be referred to in our Appendix D.4.

All the experiments are conducted on a single RTX 4090 GPU. We also provide detailed implementation of our approach and baselines in the Appendix D.2.

4.2 Mesh Reconstruction Performance

We report the quantitative results of mesh reconstruction in Table. 1 and qualitative results are shown in Fig. 4. Note that we implement ArtGS without depth supervision for a fair comparison. As can be observed, our REArtGS outperforms state-of-the-art approaches in the mean across all metrics with **3.79**, **1.236**, **0.294** and **0.695** respectively. Compared to A-SDF [21] and Ditto [9] that exploits 3D inputs for articulated object surface reconstruction, our method still achieves higher reconstruction quality in the majority of categories. In terms of PARIS, GOF and ArtGS, our approach exhibits significantly smoother and clearer surfaces as shown in Fig. 4, benefiting from our enhanced geometric constraints.

4.3 Mesh Generation Performance

We report the quantitative results of mesh generation in Table. 2 and present the qualitative results Fig. 5. Please refer to our Appendix for more qualitative results. Our REArtGS achieves the best mean results across all metrics with **4.10**, **1.063**, **0.298** and **0.670**. Compared to PARIS, our method exhibits smoother surface generation results, as shown in Fig. 5. It is mainly because PARIS lacks a reasonable geometry initiation and directly utilizes the composite rendering, leading to the spatial overlap between the neural radiation fields of the start and end states. It can be also observed that

our method is superior to ArtGS on most categories, as shown in Fig. 10 in the Appendix. This is primarily attributed to our high-quality geometry initialization from the reconstruction stage, as well as the motion-constrained deformable fields to yield dynamic generation.

Besides, we provide the part segmentation and joint parameter estimation results in the Appendix. D.5 and D.6 respectively.

Table 3: The ablation study of the unbiased SDF guidance on PartNet-Mobility dataset.

w/ SDF	w/ Unbiased Reg.	CD (ws)	CD (rs)	F1	EMD
		5.96	2.242	0.250	1.366
✓		4.38	1.921	0.273	0.817
✓	✓	3.79	1.236	0.294	0.695

4.4 Ablation Studies

We conduct an ablation of the unbiased SDF guidance on PartNet-Mobility dataset to validate its effectiveness. The ablation setting and results are reported in Table. 3. The quantitative results prove that both SDF guidance and the unbiased regularization of SDF indeed improve surface reconstruction quality. This is primarily because the SDF representation establishes explicit geometric association between the opacity fields and scene surface through Φ_k , and the unbiased SDF regularization further optimizes the distribution of Gaussian opacity fields.

We also conduct an ablation study of the motion constraints on PartNet-Mobility dataset and present the quantitative results in Table. 4. For the baseline without motion constraints, we employ three MLPs to learn the variations of spatial positions, scales, and quaternions respectively for Gaussian primitives, which is similar to D-3DGs. The significantly superior results demonstrate the effectiveness of the motion constraints.

Table 4: The ablation study of motion constraints on PartNet-Mobility dataset.

Settings	CD (ws)	CD (rs)	F1	EMD
w/o motion constraints	18.65	2.270	0.209	1.105
w/ motion constraints	5.41	1.063	0.276	0.670

Table 5: The quantitative results on real-world AKB-48 dataset. We bold the best results and underline the second best results. * means we implement it without depth supervision for fair comparison.

Category	Method	Reconstruction				Generation			
		CD(ws)↓	CD(rs)↓	F1↑	EMD↓	CD(ws)↓	CD(rs)↓	F1↑	
Box	PARIS [14]	4.69	1.651	0.097	0.843	3.98	2.131	0.306	1.055
	ArtGS* [17]	8.61	0.967	0.143	0.697	10.23	1.606	0.309	0.851
	REArtGS (Ours)	2.49	0.898	0.205	0.671	1.28	1.425	0.559	0.845
Stapler	PARIS [14]	0.23	0.104	0.551	0.165	0.47	0.198	0.546	0.194
	ArtGS* [17]	51.04	1.364	0.476	0.827	5.13	0.527	0.533	0.514
	REArtGS (Ours)	0.24	0.037	0.728	0.137	0.34	0.044	0.582	0.151
Scissor	PARIS [14]	0.18	0.302	0.710	0.314	0.18	0.329	0.424	0.310
	ArtGS* [17]	11.43	0.073	0.588	0.192	5.53	0.089	0.600	0.213
	REArtGS (Ours)	0.08	0.017	0.902	0.093	0.08	0.003	0.899	0.042
Cutter	PARIS [14]	2.56	1.371	0.570	0.202	45.02	1.684	0.309	1.183
	ArtGS* [17]	5.65	0.453	0.644	0.477	65.64	1.298	0.093	0.806
	REArtGS (Ours)	0.13	0.016	0.874	0.090	51.56	1.559	0.228	0.884
Drawer	PARIS [14]	30.63	4.568	0.062	1.577	33.94	3.865	0.091	1.430
	ArtGS* [17]	19.41	7.478	0.086	1.935	12.60	1.624	0.094	0.911
	REArtGS (Ours)	10.73	2.607	0.138	1.142	11.71	1.739	0.209	0.933
Eyeglasses	PARIS [14]	0.16	1.582	0.637	0.212	0.18	1.550	0.609	1.284
	ArtGS* [17]	27.49	1.384	0.557	0.832	12.12	1.592	0.747	0.955
	REArtGS (Ours)	0.04	0.018	0.969	0.096	0.04	1.568	0.974	0.886
Mean	PARIS [14]	6.41	1.336	0.438	0.569	13.96	1.626	0.380	0.707
	ArtGS* [17]	20.61	1.953	0.416	0.826	18.54	1.123	0.396	0.708
	REArtGS (Ours)	2.86	0.599	0.636	0.372	10.83	1.056	0.575	0.624

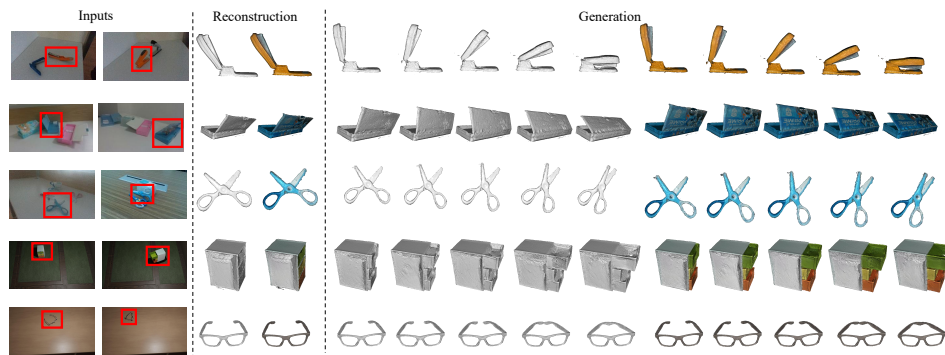


Figure 6: The qualitative results of surface reconstruction on real-world AKB-48 [15] repository. We show both textured and non-textured meshes for two-part and multi-part articulated objects.

4.5 Generalization to the Real World

We conduct reconstruction and generation experiments in the real world to investigate the generalization capacity of our REArtGS. We report the quantitative results comparing with PARIS and ArtGS in Table. 5, and present the qualitative results in Fig. 6. Our approach significantly outperforms PARIS and ArtGS in mean performance across all metrics. This demonstrates that our method exhibits strong generalization capability for real-world objects and enables high-quality surface reconstruction and generation as shown in Fig. 6.

5 Conclusion and Future Work

We propose REArtGS, a novel framework that achieves high-quality textured mesh reconstruction and dynamic generation of articulated objects using only RGB views of two arbitrary states. We propose an unbiased SDF guidance to regularize Gaussian opacity fields and model the Gaussian deformation fields constrained by kinematic structures for generating meshes of unseen states. Experiments show the superior performance of our method on both synthetic and real-world data.

The limitations of REArtGS lie on the requirement of camera pose prior and challenges of objects with transparent materials. Future works will introduce relative pose estimation to alleviate the dependence on camera poses and employ physically-based networks to model the transparent materials.

Acknowledgements

This work was supported by National Natural Science Foundation of China under Grant 62302143, 62576130, and Anhui Province’s Key Science and Technology Project 202423k09020007.

References

- [1] Danpeng Chen, Hai Li, Weicai Ye, Yifan Wang, Weijian Xie, Shangjin Zhai, Nan Wang, Haomin Liu, Hujun Bao, and Guofeng Zhang. Pgssr: Planar-based gaussian splatting for efficient and high-fidelity surface reconstruction. *IEEE Transactions on Visualization and Computer Graphics*, 2024.
- [2] Hanlin Chen, Chen Li, and Gim Hee Lee. Neusg: Neural implicit surface reconstruction with 3d gaussian splatting guidance. *arXiv preprint arXiv:2312.00846*, 2023.
- [3] Pinxuan Dai, Jiamin Xu, Wenxiang Xie, Xinguo Liu, Huamin Wang, and Weiwei Xu. High-quality surface reconstruction using gaussian surfels. In *ACM SIGGRAPH 2024 Conference Papers*, pages 1–11, 2024.
- [4] Yuanxing Duan, Fangyin Wei, Qiyu Dai, Yuhang He, Wenzheng Chen, and Baoquan Chen. 4d gaussian splatting: Towards efficient novel view synthesis for dynamic scenes. *arXiv e-prints*, pages arXiv–2402, 2024.
- [5] Amos Gropp, Lior Yariv, Niv Haim, Matan Atzmon, and Yaron Lipman. Implicit geometric regularization for learning shapes. *arXiv preprint arXiv:2002.10099*, 2020.
- [6] Antoine Guédon and Vincent Lepetit. Sugar: Surface-aligned gaussian splatting for efficient 3d mesh reconstruction and high-quality mesh rendering. In *Proceedings of the IEEE/CVF Conference on Computer Vision and Pattern Recognition*, pages 5354–5363, 2024.
- [7] Junfu Guo, Yu Xin, Gaoyi Liu, Kai Xu, Ligang Liu, and Ruizhen Hu. Articulatedgs: Self-supervised digital twin modeling of articulated objects using 3d gaussian splatting. *arXiv preprint arXiv:2503.08135*, 2025.
- [8] Binbin Huang, Zehao Yu, Anpei Chen, Andreas Geiger, and Shenghua Gao. 2d gaussian splatting for geometrically accurate radiance fields. In *ACM SIGGRAPH 2024 conference papers*, pages 1–11, 2024.
- [9] Zhenyu Jiang, Cheng-Chun Hsu, and Yuke Zhu. Ditto: Building digital twins of articulated objects from interaction. In *Proceedings of the IEEE/CVF Conference on Computer Vision and Pattern Recognition*, pages 5616–5626, 2022.
- [10] Bernhard Kerbl, Georgios Kopanas, Thomas Leimkühler, and George Drettakis. 3d gaussian splatting for real-time radiance field rendering. *ACM Trans. Graph.*, 42(4):139–1, 2023.
- [11] Jiyang Li, Lechao Cheng, Zhangye Wang, Tingting Mu, and Jingxuan He. Loopgaussian: creating 3d cinemagraph with multi-view images via eulerian motion field. In *Proceedings of the 32nd ACM International Conference on Multimedia*, pages 476–485, 2024.

- [12] Kailin Li, Jingbo Wang, Lixin Yang, Cewu Lu, and Bo Dai. Semgrasp: Semantic grasp generation via language aligned discretization. In *European Conference on Computer Vision*, pages 109–127. Springer, 2024.
- [13] Isabella Liu, Hao Su, and Xiaolong Wang. Dynamic gaussians mesh: Consistent mesh reconstruction from monocular videos. *arXiv preprint arXiv:2404.12379*, 2024.
- [14] Jiayi Liu, Ali Mahdavi-Amiri, and Manolis Savva. Paris: Part-level reconstruction and motion analysis for articulated objects. In *Proceedings of the IEEE/CVF International Conference on Computer Vision*, pages 352–363, 2023.
- [15] Liu Liu, Wenqiang Xu, Haoyuan Fu, Sucheng Qian, Qiaojun Yu, Yang Han, and Cewu Lu. Akb-48: A real-world articulated object knowledge base. In *Proceedings of the IEEE/CVF Conference on Computer Vision and Pattern Recognition*, pages 14809–14818, 2022.
- [16] Liu Liu, Han Xue, Wenqiang Xu, Haoyuan Fu, and Cewu Lu. Toward real-world category-level articulation pose estimation. *IEEE Transactions on Image Processing*, 31:1072–1083, 2022.
- [17] Yu Liu, Baoxiong Jia, Ruijie Lu, Junfeng Ni, Song-Chun Zhu, and Siyuan Huang. Building interactable replicas of complex articulated objects via gaussian splatting. In *The Thirteenth International Conference on Learning Representations*, 2025.
- [18] Xiaoyang Lyu, Yang-Tian Sun, Yi-Hua Huang, Xiuzhe Wu, Ziyi Yang, Yilun Chen, Jiangmiao Pang, and Xiaojuan Qi. 3dgsr: Implicit surface reconstruction with 3d gaussian splatting. *ACM Transactions on Graphics (TOG)*, 43(6):1–12, 2024.
- [19] Lars Mescheder, Michael Oechsle, Michael Niemeyer, Sebastian Nowozin, and Andreas Geiger. Occupancy networks: Learning 3d reconstruction in function space. In *Proceedings of the IEEE/CVF conference on computer vision and pattern recognition*, pages 4460–4470, 2019.
- [20] Ben Mildenhall, Pratul P Srinivasan, Matthew Tancik, Jonathan T Barron, Ravi Ramamoorthi, and Ren Ng. Nerf: Representing scenes as neural radiance fields for view synthesis. *Communications of the ACM*, 65(1):99–106, 2021.
- [21] Jiteng Mu, Weichao Qiu, Adam Kortylewski, Alan Yuille, Nuno Vasconcelos, and Xiaolong Wang. A-sdf: Learning disentangled signed distance functions for articulated shape representation. In *Proceedings of the IEEE/CVF International Conference on Computer Vision*, pages 13001–13011, 2021.
- [22] Richard A Newcombe, Shahram Izadi, Otmar Hilliges, David Molyneaux, David Kim, Andrew J Davison, Pushmeet Kohi, Jamie Shotton, Steve Hodges, and Andrew Fitzgibbon. Kinectfusion: Real-time dense surface mapping and tracking. In *2011 10th IEEE international symposium on mixed and augmented reality*, pages 127–136. Ieee, 2011.
- [23] Jeong Joon Park, Peter Florence, Julian Straub, Richard Newcombe, and Steven Lovegrove. Deepsdf: Learning continuous signed distance functions for shape representation. In *Proceedings of the IEEE/CVF conference on computer vision and pattern recognition*, pages 165–174, 2019.
- [24] E Piña. Rotations with rodrigues’ vector. *European journal of physics*, 32(5):1171, 2011.
- [25] Minghan Qin, Wanhua Li, Jiawei Zhou, Haoqian Wang, and Hanspeter Pfister. Langsplat: 3d language gaussian splatting. In *Proceedings of the IEEE/CVF Conference on Computer Vision and Pattern Recognition*, pages 20051–20060, 2024.
- [26] Marie-Julie Rakotosaona, Fabian Manhardt, Diego Martin Arroyo, Michael Niemeyer, Abhijit Kundu, and Federico Tombari. Nerfmeshing: Distilling neural radiance fields into geometrically-accurate 3d meshes. In *2024 international conference on 3D vision (3DV)*, pages 1156–1165. IEEE, 2024.
- [27] Jaehyeok Shim and Kyungdon Joo. Ditto: Dual and integrated latent topologies for implicit 3d reconstruction. In *Proceedings of the IEEE/CVF Conference on Computer Vision and Pattern Recognition*, pages 5396–5405, 2024.

- [28] Chaoyue Song, Jiacheng Wei, Chuan Sheng Foo, Guosheng Lin, and Fayao Liu. Reacto: Reconstructing articulated objects from a single video. In *Proceedings of the IEEE/CVF Conference on Computer Vision and Pattern Recognition*, pages 5384–5395, 2024.
- [29] Jiaxiang Tang, Hang Zhou, Xiaokang Chen, Tianshu Hu, Errui Ding, Jingdong Wang, and Gang Zeng. Delicate textured mesh recovery from nerf via adaptive surface refinement. In *Proceedings of the IEEE/CVF International Conference on Computer Vision*, pages 17739–17749, 2023.
- [30] Junbo Wang, Wenhai Liu, Qiaojun Yu, Yang You, Liu Liu, Weiming Wang, and Cewu Lu. Rpmart: Towards robust perception and manipulation for articulated objects. In *2024 IEEE/RSJ International Conference on Intelligent Robots and Systems (IROS)*, pages 7270–7277. IEEE, 2024.
- [31] Peng Wang, Lingjie Liu, Yuan Liu, Christian Theobalt, Taku Komura, and Wenping Wang. Neus: Learning neural implicit surfaces by volume rendering for multi-view reconstruction. *arXiv preprint arXiv:2106.10689*, 2021.
- [32] Fanbo Xiang, Yuzhe Qin, Kaichun Mo, Yikuan Xia, Hao Zhu, Fangchen Liu, Minghua Liu, Hanxiao Jiang, Yifu Yuan, He Wang, et al. Sapien: A simulated part-based interactive environment. In *Proceedings of the IEEE/CVF conference on computer vision and pattern recognition*, pages 11097–11107, 2020.
- [33] Haodong Xiang, Xinghui Li, Xiansong Lai, Wanting Zhang, Zhichao Liao, Kai Cheng, and Xueping Liu. Gaussianroom: Improving 3d gaussian splatting with sdf guidance and monocular cues for indoor scene reconstruction. *arXiv preprint arXiv:2405.19671*, 2024.
- [34] Han Xue, Liu Liu, Wenqiang Xu, Haoyuan Fu, and Cewu Lu. Omad: Object model with articulated deformations for pose estimation and retrieval. 2021.
- [35] Lixin Yang, Kailin Li, Xinyu Zhan, Fei Wu, Anran Xu, Liu Liu, and Cewu Lu. Oakink: A large-scale knowledge repository for understanding hand-object interaction. In *Proceedings of the IEEE/CVF conference on computer vision and pattern recognition*, pages 20953–20962, 2022.
- [36] Ziyi Yang, Xinyu Gao, Wen Zhou, Shaohui Jiao, Yuqing Zhang, and Xiaogang Jin. Deformable 3d gaussians for high-fidelity monocular dynamic scene reconstruction. In *Proceedings of the IEEE/CVF conference on computer vision and pattern recognition*, pages 20331–20341, 2024.
- [37] Mulin Yu, Tao Lu, Lining Xu, Lihan Jiang, Yuanbo Xiangli, and Bo Dai. Gsdf: 3dgs meets sdf for improved rendering and reconstruction. *arXiv preprint arXiv:2403.16964*, 2024.
- [38] Qiaojun Yu, Junbo Wang, Wenhai Liu, Ce Hao, Liu Liu, Lin Shao, Weiming Wang, and Cewu Lu. Gamma: Generalizable articulation modeling and manipulation for articulated objects. In *2024 IEEE International Conference on Robotics and Automation (ICRA)*, pages 5419–5426. IEEE, 2024.
- [39] Zehao Yu, Anpei Chen, Binbin Huang, Torsten Sattler, and Andreas Geiger. Mip-splatting: Alias-free 3d gaussian splatting. In *Proceedings of the IEEE/CVF conference on computer vision and pattern recognition*, pages 19447–19456, 2024.
- [40] Zehao Yu, Torsten Sattler, and Andreas Geiger. Gaussian opacity fields: Efficient adaptive surface reconstruction in unbounded scenes. *ACM Transactions on Graphics (TOG)*, 43(6):1–13, 2024.
- [41] Chi Zhang, Yujun Cai, Guosheng Lin, and Chunhua Shen. Deepemd: Differentiable earth mover’s distance for few-shot learning. *IEEE Transactions on Pattern Analysis and Machine Intelligence*, 45(5):5632–5648, 2022.

NeurIPS Paper Checklist

1. Claims

Question: Do the main claims made in the abstract and introduction accurately reflect the paper's contributions and scope?

Answer: [Yes]

Justification: see the *Abstract* and *Introduction* part.

Guidelines:

- The answer NA means that the abstract and introduction do not include the claims made in the paper.
- The abstract and/or introduction should clearly state the claims made, including the contributions made in the paper and important assumptions and limitations. A No or NA answer to this question will not be perceived well by the reviewers.
- The claims made should match theoretical and experimental results, and reflect how much the results can be expected to generalize to other settings.
- It is fine to include aspirational goals as motivation as long as it is clear that these goals are not attained by the paper.

2. Limitations

Question: Does the paper discuss the limitations of the work performed by the authors?

Answer: [Yes]

Justification: please see Sec. 5.

Guidelines:

- The answer NA means that the paper has no limitation while the answer No means that the paper has limitations, but those are not discussed in the paper.
- The authors are encouraged to create a separate "Limitations" section in their paper.
- The paper should point out any strong assumptions and how robust the results are to violations of these assumptions (e.g., independence assumptions, noiseless settings, model well-specification, asymptotic approximations only holding locally). The authors should reflect on how these assumptions might be violated in practice and what the implications would be.
- The authors should reflect on the scope of the claims made, e.g., if the approach was only tested on a few datasets or with a few runs. In general, empirical results often depend on implicit assumptions, which should be articulated.
- The authors should reflect on the factors that influence the performance of the approach. For example, a facial recognition algorithm may perform poorly when image resolution is low or images are taken in low lighting. Or a speech-to-text system might not be used reliably to provide closed captions for online lectures because it fails to handle technical jargon.
- The authors should discuss the computational efficiency of the proposed algorithms and how they scale with dataset size.
- If applicable, the authors should discuss possible limitations of their approach to address problems of privacy and fairness.
- While the authors might fear that complete honesty about limitations might be used by reviewers as grounds for rejection, a worse outcome might be that reviewers discover limitations that aren't acknowledged in the paper. The authors should use their best judgment and recognize that individual actions in favor of transparency play an important role in developing norms that preserve the integrity of the community. Reviewers will be specifically instructed to not penalize honesty concerning limitations.

3. Theory assumptions and proofs

Question: For each theoretical result, does the paper provide the full set of assumptions and a complete (and correct) proof?

Answer: [Yes]

Justification: please see Sec. C.1.

Guidelines:

- The answer NA means that the paper does not include theoretical results.
- All the theorems, formulas, and proofs in the paper should be numbered and cross-referenced.
- All assumptions should be clearly stated or referenced in the statement of any theorems.
- The proofs can either appear in the main paper or the supplemental material, but if they appear in the supplemental material, the authors are encouraged to provide a short proof sketch to provide intuition.
- Inversely, any informal proof provided in the core of the paper should be complemented by formal proofs provided in appendix or supplemental material.
- Theorems and Lemmas that the proof relies upon should be properly referenced.

4. Experimental result reproducibility

Question: Does the paper fully disclose all the information needed to reproduce the main experimental results of the paper to the extent that it affects the main claims and/or conclusions of the paper (regardless of whether the code and data are provided or not)?

Answer: [Yes]

Justification: Experimental settings are illustrated in Sec. D.2, and the whole project will be released after the paper is accepted.

Guidelines:

- The answer NA means that the paper does not include experiments.
- If the paper includes experiments, a No answer to this question will not be perceived well by the reviewers: Making the paper reproducible is important, regardless of whether the code and data are provided or not.
- If the contribution is a dataset and/or model, the authors should describe the steps taken to make their results reproducible or verifiable.
- Depending on the contribution, reproducibility can be accomplished in various ways. For example, if the contribution is a novel architecture, describing the architecture fully might suffice, or if the contribution is a specific model and empirical evaluation, it may be necessary to either make it possible for others to replicate the model with the same dataset, or provide access to the model. In general, releasing code and data is often one good way to accomplish this, but reproducibility can also be provided via detailed instructions for how to replicate the results, access to a hosted model (e.g., in the case of a large language model), releasing of a model checkpoint, or other means that are appropriate to the research performed.
- While NeurIPS does not require releasing code, the conference does require all submissions to provide some reasonable avenue for reproducibility, which may depend on the nature of the contribution. For example
 - (a) If the contribution is primarily a new algorithm, the paper should make it clear how to reproduce that algorithm.
 - (b) If the contribution is primarily a new model architecture, the paper should describe the architecture clearly and fully.
 - (c) If the contribution is a new model (e.g., a large language model), then there should either be a way to access this model for reproducing the results or a way to reproduce the model (e.g., with an open-source dataset or instructions for how to construct the dataset).
 - (d) We recognize that reproducibility may be tricky in some cases, in which case authors are welcome to describe the particular way they provide for reproducibility. In the case of closed-source models, it may be that access to the model is limited in some way (e.g., to registered users), but it should be possible for other researchers to have some path to reproducing or verifying the results.

5. Open access to data and code

Question: Does the paper provide open access to the data and code, with sufficient instructions to faithfully reproduce the main experimental results, as described in supplemental material?

Answer: [Yes]

Justification: please see the zip files of codes in the supplemental material.

Guidelines:

- The answer NA means that paper does not include experiments requiring code.
- Please see the NeurIPS code and data submission guidelines (<https://nips.cc/public/guides/CodeSubmissionPolicy>) for more details.
- While we encourage the release of code and data, we understand that this might not be possible, so “No” is an acceptable answer. Papers cannot be rejected simply for not including code, unless this is central to the contribution (e.g., for a new open-source benchmark).
- The instructions should contain the exact command and environment needed to run to reproduce the results. See the NeurIPS code and data submission guidelines (<https://nips.cc/public/guides/CodeSubmissionPolicy>) for more details.
- The authors should provide instructions on data access and preparation, including how to access the raw data, preprocessed data, intermediate data, and generated data, etc.
- The authors should provide scripts to reproduce all experimental results for the new proposed method and baselines. If only a subset of experiments are reproducible, they should state which ones are omitted from the script and why.
- At submission time, to preserve anonymity, the authors should release anonymized versions (if applicable).
- Providing as much information as possible in supplemental material (appended to the paper) is recommended, but including URLs to data and code is permitted.

6. Experimental setting/details

Question: Does the paper specify all the training and test details (e.g., data splits, hyperparameters, how they were chosen, type of optimizer, etc.) necessary to understand the results?

Answer: [Yes]

Justification: please see Sec. D.2.

Guidelines:

- The answer NA means that the paper does not include experiments.
- The experimental setting should be presented in the core of the paper to a level of detail that is necessary to appreciate the results and make sense of them.
- The full details can be provided either with the code, in appendix, or as supplemental material.

7. Experiment statistical significance

Question: Does the paper report error bars suitably and correctly defined or other appropriate information about the statistical significance of the experiments?

Answer: [No]

Justification: the effect of random seed could almost be negligible since we set the same initiation seed during experiments. Reproducibility can be guaranteed.

Guidelines:

- The answer NA means that the paper does not include experiments.
- The authors should answer "Yes" if the results are accompanied by error bars, confidence intervals, or statistical significance tests, at least for the experiments that support the main claims of the paper.
- The factors of variability that the error bars are capturing should be clearly stated (for example, train/test split, initialization, random drawing of some parameter, or overall run with given experimental conditions).
- The method for calculating the error bars should be explained (closed form formula, call to a library function, bootstrap, etc.)
- The assumptions made should be given (e.g., Normally distributed errors).

- It should be clear whether the error bar is the standard deviation or the standard error of the mean.
- It is OK to report 1-sigma error bars, but one should state it. The authors should preferably report a 2-sigma error bar than state that they have a 96% CI, if the hypothesis of Normality of errors is not verified.
- For asymmetric distributions, the authors should be careful not to show in tables or figures symmetric error bars that would yield results that are out of range (e.g. negative error rates).
- If error bars are reported in tables or plots, The authors should explain in the text how they were calculated and reference the corresponding figures or tables in the text.

8. Experiments compute resources

Question: For each experiment, does the paper provide sufficient information on the computer resources (type of compute workers, memory, time of execution) needed to reproduce the experiments?

Answer: [Yes]

Justification: please see the Sec. D.2.

Guidelines:

- The answer NA means that the paper does not include experiments.
- The paper should indicate the type of compute workers CPU or GPU, internal cluster, or cloud provider, including relevant memory and storage.
- The paper should provide the amount of compute required for each of the individual experimental runs as well as estimate the total compute.
- The paper should disclose whether the full research project required more compute than the experiments reported in the paper (e.g., preliminary or failed experiments that didn't make it into the paper).

9. Code of ethics

Question: Does the research conducted in the paper conform, in every respect, with the NeurIPS Code of Ethics <https://neurips.cc/public/EthicsGuidelines>?

Answer: [Yes]

Justification: we have conformed with the NeurIPS Code of Ethics.

Guidelines:

- The answer NA means that the authors have not reviewed the NeurIPS Code of Ethics.
- If the authors answer No, they should explain the special circumstances that require a deviation from the Code of Ethics.
- The authors should make sure to preserve anonymity (e.g., if there is a special consideration due to laws or regulations in their jurisdiction).

10. Broader impacts

Question: Does the paper discuss both potential positive societal impacts and negative societal impacts of the work performed?

Answer:[Yes]

Justification: Please see Sec. 1.

Guidelines:

- The answer NA means that there is no societal impact of the work performed.
- If the authors answer NA or No, they should explain why their work has no societal impact or why the paper does not address societal impact.
- Examples of negative societal impacts include potential malicious or unintended uses (e.g., disinformation, generating fake profiles, surveillance), fairness considerations (e.g., deployment of technologies that could make decisions that unfairly impact specific groups), privacy considerations, and security considerations.

- The conference expects that many papers will be foundational research and not tied to particular applications, let alone deployments. However, if there is a direct path to any negative applications, the authors should point it out. For example, it is legitimate to point out that an improvement in the quality of generative models could be used to generate deepfakes for disinformation. On the other hand, it is not needed to point out that a generic algorithm for optimizing neural networks could enable people to train models that generate Deepfakes faster.
- The authors should consider possible harms that could arise when the technology is being used as intended and functioning correctly, harms that could arise when the technology is being used as intended but gives incorrect results, and harms following from (intentional or unintentional) misuse of the technology.
- If there are negative societal impacts, the authors could also discuss possible mitigation strategies (e.g., gated release of models, providing defenses in addition to attacks, mechanisms for monitoring misuse, mechanisms to monitor how a system learns from feedback over time, improving the efficiency and accessibility of ML).

11. Safeguards

Question: Does the paper describe safeguards that have been put in place for responsible release of data or models that have a high risk for misuse (e.g., pretrained language models, image generators, or scraped datasets)?

Answer: [NA]

Justification: this work poses no such risks.

Guidelines:

- The answer NA means that the paper poses no such risks.
- Released models that have a high risk for misuse or dual-use should be released with necessary safeguards to allow for controlled use of the model, for example by requiring that users adhere to usage guidelines or restrictions to access the model or implementing safety filters.
- Datasets that have been scraped from the Internet could pose safety risks. The authors should describe how they avoided releasing unsafe images.
- We recognize that providing effective safeguards is challenging, and many papers do not require this, but we encourage authors to take this into account and make a best faith effort.

12. Licenses for existing assets

Question: Are the creators or original owners of assets (e.g., code, data, models), used in the paper, properly credited and are the license and terms of use explicitly mentioned and properly respected?

Answer: [Yes]

Justification: please see the main manuscript.

Guidelines:

- The answer NA means that the paper does not use existing assets.
- The authors should cite the original paper that produced the code package or dataset.
- The authors should state which version of the asset is used and, if possible, include a URL.
- The name of the license (e.g., CC-BY 4.0) should be included for each asset.
- For scraped data from a particular source (e.g., website), the copyright and terms of service of that source should be provided.
- If assets are released, the license, copyright information, and terms of use in the package should be provided. For popular datasets, paperswithcode.com/datasets has curated licenses for some datasets. Their licensing guide can help determine the license of a dataset.
- For existing datasets that are re-packaged, both the original license and the license of the derived asset (if it has changed) should be provided.

- If this information is not available online, the authors are encouraged to reach out to the asset's creators.

13. New assets

Question: Are new assets introduced in the paper well documented and is the documentation provided alongside the assets?

Answer: [NA]

Justification: this work does not release new assets.

Guidelines:

- The answer NA means that the paper does not release new assets.
- Researchers should communicate the details of the dataset/code/model as part of their submissions via structured templates. This includes details about training, license, limitations, etc.
- The paper should discuss whether and how consent was obtained from people whose asset is used.
- At submission time, remember to anonymize your assets (if applicable). You can either create an anonymized URL or include an anonymized zip file.

14. Crowdsourcing and research with human subjects

Question: For crowdsourcing experiments and research with human subjects, does the paper include the full text of instructions given to participants and screenshots, if applicable, as well as details about compensation (if any)?

Answer: [NA]

Justification: This work does not involve crowdsourcing nor research with human subjects.

Guidelines:

- The answer NA means that the paper does not involve crowdsourcing nor research with human subjects.
- Including this information in the supplemental material is fine, but if the main contribution of the paper involves human subjects, then as much detail as possible should be included in the main paper.
- According to the NeurIPS Code of Ethics, workers involved in data collection, curation, or other labor should be paid at least the minimum wage in the country of the data collector.

15. Institutional review board (IRB) approvals or equivalent for research with human subjects

Question: Does the paper describe potential risks incurred by study participants, whether such risks were disclosed to the subjects, and whether Institutional Review Board (IRB) approvals (or an equivalent approval/review based on the requirements of your country or institution) were obtained?

Answer: [NA]

Justification: this work does not involve crowdsourcing nor research with human subjects.

Guidelines:

- The answer NA means that the paper does not involve crowdsourcing nor research with human subjects.
- Depending on the country in which research is conducted, IRB approval (or equivalent) may be required for any human subjects research. If you obtained IRB approval, you should clearly state this in the paper.
- We recognize that the procedures for this may vary significantly between institutions and locations, and we expect authors to adhere to the NeurIPS Code of Ethics and the guidelines for their institution.
- For initial submissions, do not include any information that would break anonymity (if applicable), such as the institution conducting the review.

16. Declaration of LLM usage

Question: Does the paper describe the usage of LLMs if it is an important, original, or non-standard component of the core methods in this research? Note that if the LLM is used only for writing, editing, or formatting purposes and does not impact the core methodology, scientific rigorosity, or originality of the research, declaration is not required.

Answer: [NA]

Justification: this work does not involve LLMs as any important, original, or non-standard components.

Guidelines:

- The answer NA means that the core method development in this research does not involve LLMs as any important, original, or non-standard components.
- Please refer to our LLM policy (<https://neurips.cc/Conferences/2025/LLM>) for what should or should not be described.

Appendix

A Overview

In the appendix, we first provide a detailed comparison highlighting our advantages over related works in Sec. B. Then we elaborately extend our method in Sec. C from the following four aspects: unbiased SDF guidance theory, textured mesh extraction, joint type prediction, and multi-joint mesh generation. In addition, more experimental details and results are presented in Sec.D. Finally, we provide our codes and video in Sec. E.

B Related Work, Extended

Recently several methods also attempt to integrate SDF representation with 3D Gaussian primitives [37, 2, 33, 3, 18] and have improved surface reconstruction quality. However, most approaches are limited to normal regularization and pruning strategy of Gaussian primitives through SDF representation [37, 2, 33, 3], and the opacity of Gaussian primitives holds a more essential role in the α -blending. In contrast, we leverage the unbiased SDF guidance to regularize Gaussian opacity fields, achieving substantial geometric constraints and enhancing geometric optimization. 3DGSR [18] directly obtains the opacity of Gaussian primitives through SDF-opacity conversion proposed in Neus [31] and also employs a bell-shaped activation function to control the distribution of SDF-opacity. Nevertheless, since the SDF network simply utilizes Gaussian’s center as input, 3DGSR ignores the local features of Gaussian primitives. In comparison, our approach combines the local rendering contributions with SDF-opacity conversation results as Gaussian’s opacity values, yielding more reasonable distribution of Gaussian opacity fields.

Most recently, ArtGS [17] also proposes a mesh reconstruction method for articulated objects. Although demonstrating its effectiveness and robustness for mesh reconstruction, it relies on depth inputs, limiting its performance when the 3D supervision is unavailable. Moreover, it still lacks sufficient geometry constraints, leading to noisy results occasionally. In contrast, our REArtGS only requires 2D RGB images as inputs and introduces additional geometry constraints, improving the mesh reconstruction quality.

C Methodology, Extended

C.1 Unbiased SDF Guidance for Gaussian Opacity Fields, Extended

As defined in the main draft, the opacity of Gaussian primitives combines with the rendering contribution ε , formulated as:

$$\begin{aligned} \sigma_i &= \hat{\sigma}_i \varepsilon \\ &= \hat{\sigma}_i \cdot \max \left(e^{-\frac{1}{2}(\mathbf{r}_L^T \mathbf{r}_L t^2 + 2\mathbf{o}_L^T \mathbf{r}_L t + \mathbf{o}_L^T \mathbf{o}_L)} \right) \end{aligned} \quad (19)$$

where $\mathbf{x}_L = \mathbf{o}_L + t\mathbf{r}_L$. \mathbf{x}_L , \mathbf{o}_L , \mathbf{r}_L represent the spatial position, camera center, and ray direction of Gaussian’s local coordinate system respectively. ε attain its maximum value when $t = t^*$ as mentioned in the main draft. $\hat{\sigma}_i$ can be derived from Φ_k and the SDF-opacity conversation, where Φ_k is also defined in the main draft, formulated as:

$$\Phi_k(f(\mathbf{x})) = \frac{e^{k \cdot f(\mathbf{x})}}{(1 + e^{k \cdot f(\mathbf{x})})^2} \quad (20)$$

Although the composite function $\hat{\sigma}(f(\mathbf{x}))$ attains its maximum when $f(\mathbf{x}) = 0$, a non-alignment still exists between the maximum points, formulated as:

$$\hat{t} = \operatorname{argmax}(\hat{\sigma}(\mathbf{x}(t))) \not\Rightarrow \hat{t} = t^* \quad (21)$$

This mismatch leads to a spatial deviation between $\hat{\sigma}$ and ε proposed in the main draft:

$$t_{\text{bias}} = \left\| \operatorname{argmax}_t(\hat{\sigma}) - \operatorname{argmax}_t(\varepsilon) \right\| \quad (22)$$

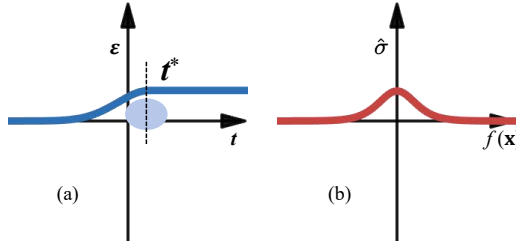


Figure 7: The distribution of $t-\varepsilon$ (a) and SDF- $\hat{\sigma}_i$ (b) without the unbiased SDF regularization.

As illustrated in the main draft (Fig. 3), the deviation t_{bias} results in a disordered distribution of the Gaussian opacity fields. We also present their distributions without regularization for intuitive illustration in Fig. 7.

To tackle the deviation, we propose an unbiased SDF regularization \mathcal{L}_{unbias} defined in the main draft:

$$\mathcal{L}_{unbias} = \|f(\mathbf{o} + t^*\mathbf{r})\|_2^2 \quad (23)$$

We present the theorem and proof that \mathcal{L}_{unbias} is capable of eliminating the deviation t_{bias} in Theorem. 1 and Proof. 1 below.

Theorem 1 Let $f : \mathbb{R}^3 \rightarrow \mathbb{R}$ be a multilayer perceptron (MLP) with smooth activation functions, and let the spatial position be defined as $\mathbf{x}(t) = \mathbf{o} + t\mathbf{r}$ with camera center $\mathbf{o} \in \mathbb{R}^3$ and ray direction $\mathbf{r} \in \mathbb{R}^3$. Let $\underset{t}{\operatorname{argmax}}(\varepsilon) = t^*$. Consider the activation function $\Phi_k : \mathbb{R} \rightarrow \mathbb{R}$ defined by:

$$\Phi_k(z) = \frac{e^{kz}}{(1 + e^{kz})^2}, \quad k > 0 \quad (24)$$

If $\lim_{t \rightarrow t^*} f(\mathbf{x}(t)) = 0$, then the composite function $\Phi_k \circ f \circ \mathbf{x}(t)$ attains its maximum at $t = t^*$, i.e., $\left\| \underset{t}{\operatorname{argmax}}(\hat{\sigma}) - \underset{t}{\operatorname{argmax}}(\varepsilon) \right\| = 0$.

Proof 1 Define $z(t) := f(\mathbf{x}(t))$. Compute the first derivative:

$$\begin{aligned} \frac{d\Phi_k}{dz} &= \frac{d}{dz} \left(\frac{e^{kz}}{(1 + e^{kz})^2} \right) \\ &= \frac{ke^{kz}(1 + e^{kz})^2 - 2ke^{kz}e^{kz}(1 + e^{kz})}{(1 + e^{kz})^4} \\ &= \frac{ke^{kz}(1 - e^{kz})}{(1 + e^{kz})^3} \end{aligned}$$

Setting $\frac{d\Phi_k}{dz} = 0$ gives the unique critical point at $z = 0$.

Evaluate the second derivative at $z = 0$:

$$\begin{aligned} \frac{d^2\Phi_k}{dz^2} \Big|_{z=0} &= \frac{k^2 e^{kz}(1 - 4e^{kz} + e^{2kz})}{(1 + e^{kz})^4} \Big|_{z=0} \\ &= \frac{k^2(-4)}{16} = -\frac{k^2}{4} < 0 \end{aligned}$$

For $z > 0$, $\frac{d\Phi_k}{dz} < 0$; for $z < 0$, $\frac{d\Phi_k}{dz} > 0$. This proves that the maximum value of Φ_k is attained when $z(t) = 0$. Given that $\lim_{t \rightarrow t^*} f(\mathbf{x}(t)) = 0$ and $\underset{t}{\operatorname{argmax}}(\varepsilon) = t^*$, it can be proved that

$$\left\| \underset{t}{\operatorname{argmax}}(\hat{\sigma}) - \underset{t}{\operatorname{argmax}}(\varepsilon) \right\| = 0.$$

C.2 Textured Mesh Extraction, Extended

In this paper, we employ TSDF fusion [22] to extract textured meshes from the regularized Gaussian opacity fields. We first obtain multi-view RGB renderings through α -blending, where the opacity σ and view-dependent spherical harmonics (SH) coefficients jointly modulate the color accumulation. These per-pixel blended colors are then projected into the voxel block grid (VBG), ensuring that high-opacity regions dominate the color field, while low-opacity areas are suppressed. Meanwhile, we acquire the multi-view depth renderings via α -blending and conduct filtration with a minimum opacity threshold 0.5 as well as a maximum depth threshold 5.0. Then the filtered depth renderings are similarly integrated into the VBG. After multi-view fusion, a triangle mesh is extracted via Marching Cubes and vertex colors are directly sampled from the VBG’s color fields. This process effectively bakes the fused texture into the extracted mesh.

In the early experiments, we also attempt to use SDF combined with Marching Tetrahedra to extract surface meshes, but this leads to a decline in surface quality. It is mainly because the SDF-opacity conversion only uses the center positions of Gaussian primitives for approximate calculation during training. Therefore, the SDF network only learns the spatial information at Gaussian’s center, making it challenging to handle dense sampling points in mesh extraction. In contrast, the α -blending in TSDF fusion incorporates the local information of the Gaussian primitives via Gaussian opacity fields, yielding higher-quality mesh results.

C.3 Joint Type Prediction

Given an articulated object with unknown kinematic structure, we first obtain two coarse point clouds \mathbf{P}_0 and \mathbf{P}_1 using the multi-view images from two states s_0 and s_1 respectively, based on the proposed pipeline in Sec. 3.1. Note that it only takes few minutes since the training process only undergoes 3000 iterations. Then we use the Farthest Point Sampling (FPS) to produce the sparse point clouds \mathbf{P}_0^* and \mathbf{P}_1^* for \mathbf{P}_0 and \mathbf{P}_1 . For each point $p_i \in \mathbf{P}_0^*$, we identify a point $q_i \in \mathbf{P}_1^*$ closest to it. Subsequently, we filter out the dynamic points \mathbf{D} with significant displacement through the distance between p and q , formulated as:

$$\mathbf{D} = \{p_i | \|p_i - q_i\| > \tau\} \quad (25)$$

where τ is the dynamic threshold.

After that, we determine the motion type of the dynamic point set \mathbf{D} through the variance $\sigma_{\mathbf{D}}$ of the displacement direction angle.

$$\sigma_{\mathbf{D}} = \frac{1}{|\mathbf{D}|} \sum_i \left\| \arccos \left(\frac{\mathbf{v}_i \cdot \mathbf{v}_{\text{mean}}}{\|\mathbf{v}_i\| \|\mathbf{v}_{\text{mean}}\|} \right) \right\|^2 \quad (26)$$

where $\mathbf{v}_i = p_i - q_i$ and $\mathbf{v}_{\text{mean}} = \frac{1}{|\mathbf{D}|} \sum \mathbf{v}_i$. Then we use a threshold σ_{rot} to predict the motion type, that is, the joint type of the articulated object. Concretely, we determine the dynamic part as prismatic joint if $\sigma_{\mathbf{D}} \leq \sigma_{\text{rot}}$ and as rotation joint in unsatisfactory cases.

C.4 Mesh Generation of Multi-Part Articulated Object

Mesh generation of multi-part articulated objects can be treated as a straightforward extension of the two-part task for our approach. We can generate meshes for multi-part objects in unseen states through a sequentially learning strategy. Specifically, given an articulated object with k dynamic parts ω_{d_k} , we start with fixing parts $\{\omega_{d_2}, \dots, \omega_{d_k}\}$ except for the dynamic part ω_{d_1} , and the object can be decomposed into dynamic part ω_{d_1} and static part ω_s (all the remaining points). After learning the motion and segmentation mask for ω_{d_1} , we sequentially perceive dynamic part ω_{d_2} , while the static part ω_s can be updated as: $\omega_s = \hat{\omega}_{d_2} - \omega_{d_1}$, where $\hat{\omega}_{d_2}$ denotes the remaining points except ω_{d_2} . By parity of reasoning, we achieve learning all motions and segmentation masks for the k parts, and the mesh generation results for any unseen state can be obtained using the proposed pipeline in Sec. 3.2.

D Experiments, Extended

D.1 Dataset

The PartNet-Mobility dataset [32] is a synthetic dataset comprising articulated objects across 46 categories, characterized by a diverse scale and geometry. Following PARIS, we selected the same 10 categories for our experiments. Each category comprises 64 to 100 RGB views at two arbitrary states, which are sampled randomly from their upper hemispheres. AKB-48 [15] is a real-world dataset containing an extensive collection of articulated objects scanned in real indoor scenes. We select 6 categories with both two-part and multi-part objects and sample 100 RGB views at two arbitrary states for each object.

D.2 Implementation

All the experiments are conducted on a single RTX 4090 GPU. Our approach constitutes a two-stage procedure to perform surface reconstruction and generation respectively. For the reconstruction stage, we train the 3D Gaussian primitives with SDF network for 3,1000 iterations, which includes an warm-up phase consisting of 1,000 iterations for SDF initial learning. Then we employ the unbiased SDF regularization in 1,500 to 1,6000 iterations, use the SDF-normal regularization and Eikonal regularization during the entire training process. We perform the densification and pruning for 3D Gaussian primitives from 1,500 iterations to 16,000 iterations. The training time of reconstruction stage is about 60 minutes.

For the generation stage, we leverage the 3D Gaussian primitives optimized from the reconstruction stage as initialization. We also set a warm-up phase with 3,000 iterations to train 3D Gaussian primitives only using RGB images from the end state. Then we start to evaluate dynamic parts of the articulated object and apply the deformation fields to them. For the prismatic joints, we set the initial translation axis \mathbf{d} to $(1 \times 10^{-6}, 1 \times 10^{-6}, 1 \times 10^{-6})$ and set the initial translation distance m to 0.1. As for the rotation joints, we set the initial pivot point \mathbf{o}_r to $(0, 0, 0)$ and use the initial angle $\theta = 0.1$ and rotation axis $\mathbf{a} = (1, 1, 1)$ to build the initial quaternion \mathbf{q} . The total number of training iterations during the generation stage is 30,000. The training time of the generation stage is about 10 minutes and the total training time for surface generation from scratch is approximately 70 minutes.

We also present an accelerated version of REArtGS. Specifically, we approximate Δx as $\frac{z_{\text{far}} - z_{\text{near}}}{l}$ in Eq. 3, where l is set to 64. Moreover, we use Tiny-cuda-nn to accelerate the SDF network. These accelerations reduce the reconstruction time to approximately 30 minutes with almost no impact on performance.

D.3 Baselines

For the surface reconstruction experiments of articulated objects, we define the start states of articulated objects as reconstruction targets, and compare the reconstruction results with existing state-of-the-art methods: A-SDF [21], Ditto [27], PARIS [14], GOF [40] and ArtGS [17]. Note that we implement ArtGS without depth supervision for a fair comparison. In particular, A-SDF uses sampled point clouds as inputs and Ditto requires both point clouds and united robotics description format (URDF) files of articulated objects. Following PARIS, we train A-SDF on the 10 categories of the PartNet-Mobility dataset and employ the pretrained weights of Ditto to conduct the comparison.

As for the surface generation experiments, we compare the surface generation results with existing state-of-the-art methods: A-SDF, PARIS, Deformable-3DGS (D-3DGS) [36] and ArtGS [17]. Since the ground truth point clouds of unseen states are unavailable, we take the end states of the articulated objects as generation targets and generate surface meshes from the canonical states. Besides, all the methods employ point clouds (A-SDF) or RGB images (PARIS, D-3DGS, ArtGS, ours) from both start and end states as training inputs.

D.4 Metrics, Extended

We employ CD (ws), CD (rs), F1-score, EMD as the metrics of surface quality. We present the detailed calculation below.

The CD (ws) is defined as the mean of the shortest distance between two point clouds, which can be formulated as following:

$$\begin{aligned} \text{CD (ws)} = & \frac{1}{2} \left(\frac{1}{N_1} \sum_{\mathbf{x} \in N_1} \min_{\mathbf{y} \in N_2} \|\mathbf{x} - \mathbf{y}\|_2^2 \right. \\ & \left. + \frac{1}{N_2} \sum_{\mathbf{y} \in N_2} \min_{\mathbf{x} \in N_1} \|\mathbf{y} - \mathbf{x}\|_2^2 \right) \end{aligned} \quad (27)$$

where N_1, N_2 represent the point number of output and ground truth respectively. The CD (rs) is calculated by the sampled point clouds from the fragments between the rays cast by test cameras and the surface mesh, shown as following:

$$\begin{aligned} \text{CD (rs)} = & \frac{1}{2} \left(\frac{1}{N_{s_1}} \sum_{\mathbf{x} \in N_{s_1}} \min_{\mathbf{y} \in N_{s_2}} \|\mathbf{x} - \mathbf{y}\|_2^2 \right. \\ & \left. + \frac{1}{N_{s_2}} \sum_{\mathbf{y} \in N_{s_2}} \min_{\mathbf{x} \in N_{s_1}} \|\mathbf{y} - \mathbf{x}\|_2^2 \right) \end{aligned} \quad (28)$$

where N_{s_1}, N_{s_2} denote the point number of sampled output and sampled ground truth respectively. Similarly, we adopt the same point cloud sampling method to calculate EMD score [41], which can be formulated as:

$$\text{EMD}(N_{s_1}, N_{s_2}) = \min_{\phi: N_{s_1} \rightarrow N_{s_2}} \frac{1}{|N_{s_1}|} \sum_{x \in N_{s_1}} \|\mathbf{x} - \phi(\mathbf{x})\| \quad (29)$$

where ϕ is a bijection to identify the optimal correspondence between two point clouds.

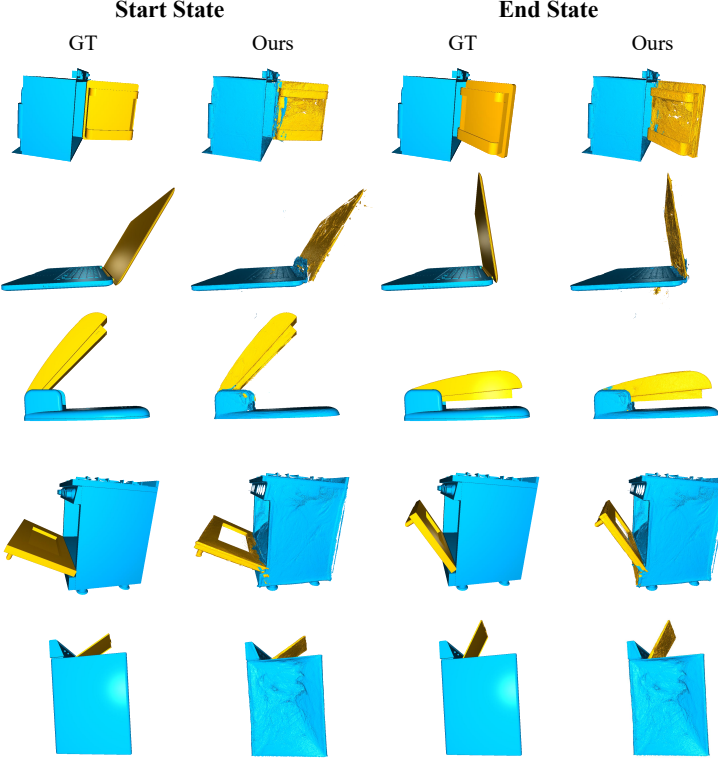


Figure 8: The qualitative results of part segmentation. We set the dynamic parts to yellow and the static parts to blue.

F1-score is the harmonic mean between the precision $P(d)$ and recall $R(d)$ with distance threshold $d = 0.4$ in this paper, formulated as:

$$F_1 = \frac{2P(d)R(d)}{P(d) + R(d)} \quad (30)$$

D.5 Part Segmentation

We present the quantitative results of part reconstruction quality on PartNet-Mobility dataset in Table. 6, and provide the qualitative results of part segmentation in Fig. 8. Our method achieves the best mean results on both dynamic and static parts. It can be also observed that our REArtGS successfully acquires accurate part decompositions, as shown in Fig. 8. This demonstrates that our approach is capable of perceiving motion, and enables accurate part segmentation using the simple yet effective heuristic method.

Table 6: Quantitative results for the part reconstruction quality on PartNet-Mobility dataset. CD-s ↓ and CD-m ↓ represent the CD results of static part and dynamic part respectively. We bold the best results and underline the second best results.

Metrics	Method	Stapler	USB	Scissor	Fridge	Foldchair	Washer	Blade	Laptop	Oven	Storage	Mean
CD-s ↓	Ditto [9]	2.38	2.09	1.70	2.16	6.80	7.29	42.04	0.31	2.51	3.91	7.19
	PARIS [14]	0.96	1.80	0.30	2.68	0.42	18.31	0.46	0.25	6.07	8.12	3.94
	ArtGS [17]	3.45	2.05	0.57	2.03	0.16	20.97	0.44	0.76	9.20	13.51	5.31
	REArtGS (Ours)	<u>1.47</u>	0.82	0.25	1.53	<u>0.31</u>	13.04	0.69	0.48	6.59	<u>7.30</u>	3.25
CD-m ↓	Ditto [9]	31.21	15.88	20.68	0.99	141.11	12.89	195.93	0.19	0.94	2.20	42.20
	PARIS [14]	0.85	0.89	0.23	1.13	<u>0.53</u>	0.27	<u>5.13</u>	0.14	<u>0.43</u>	20.67	3.06
	ArtGS [17]	2.78	1.17	0.67	1.43	0.57	2.82	1.80	0.99	2.12	7.18	<u>2.15</u>
	REArtGS (Ours)	<u>1.18</u>	0.40	0.21	0.66	0.30	<u>0.42</u>	1.97	0.11	0.25	<u>12.39</u>	1.79

D.6 Joint Parameter Estimation

We also present the joint parameter estimation quantitative results in Table. 7 and qualitative results in Fig. 9 to evaluate motion learning. Following PARIS [14], we compute the orientation error (Ang Err) between the predicted axis direction (\mathbf{a} , \mathbf{d} in our method) and the ground truth, and evaluate the position error (Pos Err) for revolute joints through the position difference of the pivot point (\mathbf{o}_r in our method). It can be observed that our method achieves the best results, which demonstrates our superiority in motion learning and further demonstrates the high fidelity of our dynamic generation.



Figure 9: The qualitative results of joint parameter estimation. We show the textured mesh with red arrow representing joint axis.

Table 7: Quantitative results for the joint parameter estimation on PartNet-Mobility dataset. Note that, - denotes the absence results for prismatic joints. We bold the best results and underline the second best results.

Metrics	Method	Stapler	USB	Scissor	Fridge	Foldchair	Washer	Oven	Laptop	Blade	Storage	Mean
Ang Err ↓	Ditto [9]	89.86	89.77	4.498	89.30	89.35	89.51	0.955	3.124	6.319	79.54	54.22
	PARIS [14]	0.069	0.065	0.019	0.001	0.020	0.082	0.028	0.034	0.001	0.369	0.069
	ArtGS [17]	<u>0.062</u>	0.034	0.039	0.038	0.048	<u>0.081</u>	0.066	0.052	0.072	0.020	0.051
	REArtGS (Ours)	0.042	<u>0.059</u>	0.010	<u>0.006</u>	<u>0.013</u>	0.067	<u>0.031</u>	0.012	<u>0.005</u>	<u>0.201</u>	0.045
Pos Err ↓	Ditto [9]	0.201	5.409	5.698	1.021	3.768	0.661	0.129	0.014	-	-	2.113
	PARIS [14]	<u>0.006</u>	0.000	0.000	<u>0.002</u>	<u>0.004</u>	0.020	0.003	0.001	-	-	0.005
	ArtGS [17]	0.011	<u>0.002</u>	<u>0.001</u>	0.003	0.000	<u>0.017</u>	<u>0.004</u>	0.001	-	-	0.004
	REArtGS (Ours)	0.002	0.000	0.000	0.000	0.006	0.011	<u>0.004</u>	0.003	-	-	0.003

D.7 Mesh Generation, Extended

To present our generation results more comprehensively, we provide the qualitative results in Fig. 10 corresponding to Table. 2 in the main draft. We generate surface meshes of the end state from the canonical state using the Gaussian deformation fields. It can be observed that our generated results still maintain smooth and high-quality surfaces, which proves the effectiveness of our method.

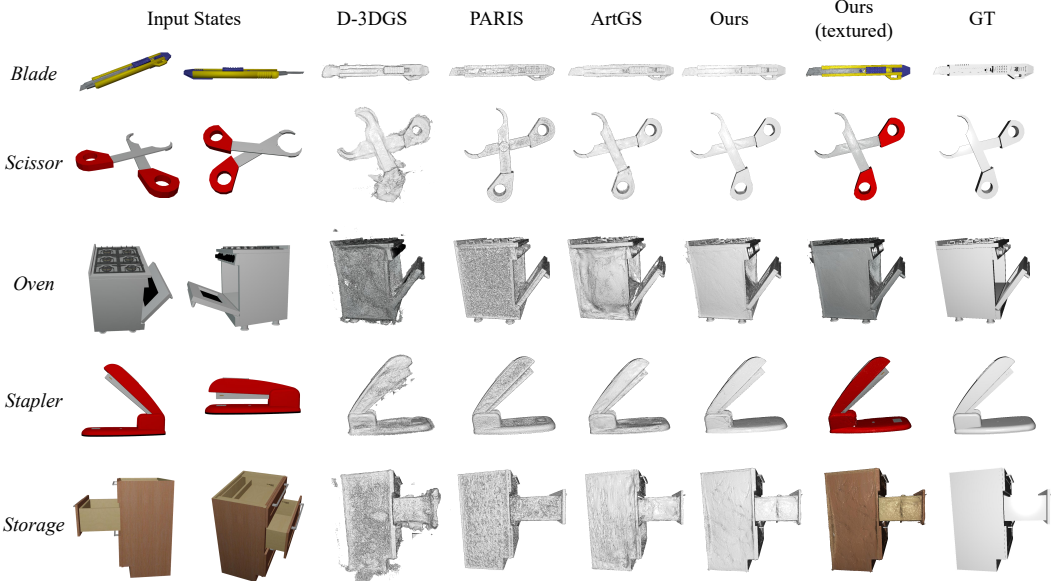


Figure 10: The qualitative results of surface generation on PartNet-Mobility dataset. We employ the deformable fields to generate surface meshes at the end state from the canonical state.

D.8 Computational Efficiency Analysis for Mesh Generation

We present the detailed training time in Sec. D.2, and also provide the qualitative inference time for mesh generation in Table. 8. It can be observed that our method achieves the highest computational efficiency. This is mainly because of our efficient design for the learnable motion parameters, which obviates inference of deep networks.

Table 8: The qualitative results of inference time for mesh generation on PartNet-Mobility dataset. The results are derived from the average of more than ten inference times.

Method	Time (second) ↓
Ditto [9]	36
D-3DGS [36]	40
PARIS [14]	33
REArtGS (Ours)	21

D.9 Ablation Study, Extended

Table 9: The ablation study of canonical state setting on PartNet-Mobility dataset.

Joint	Canonical	CD (ws)	CD (rs)	F1	EMD
Prismatic	0.0	3.54	0.717	0.280	0.573
	0.5	5.69	1.203	0.242	0.608
	1.0	6.10	1.304	0.236	0.591
Revolute	0.0	5.93	1.352	0.266	0.637
	0.5	5.88	1.150	0.275	0.556
	1.0	7.13	1.591	0.194	0.680

To evaluate the effectiveness of the canonical state selecting, we compare the surface generation quality under three settings of canonical state 0.0, 0.5, and 1.0 on PartNet-Mobility dataset. The quantitative results can be found in Table. 9. For prismatic joints, the surface reconstruction quality attains the highest when the canonical state is 0.0. It is mainly because the linear interpolation can be performed more stably taking advantage of the vector space structure of Euclidean geometry.

As for revolute joints, setting canonical state 0.5 achieves the best surface generation quality. This can be mainly attributed to the fact that canonical state 0.5 leads to the angle-bounded parameterization $\theta \in [-\pi/2, \pi/2]$, which can prevent the singularity in exponential coordinates when $\|\theta\| > \pi$.

E Reproducibility and Video

We provide our codes in <https://github.com/wd-ustc-cs/REArtGS> and present a video to show more visualization results in <https://sites.google.com/view/reartgs/home>.